Present state and perspectives of synchrotron radiation diffraction imaging

J. Baruchel, J. Härtwig* and P. Pernot-Rejmánková

European Synchrotron Radiation Facility, BP 220, 38043 Grenoble, France. E-mail: haertwig@esrf.fr

The modern third-generation synchrotron radiation sources offer enhanced possibilities for all variants of imaging techniques. The quantitative and qualitative improvements with respect to previous synchrotron diffraction imaging work, which include the investigation in transmission of bulky samples, the use, as an additional parameter, of the sample-to-detector distance, and the use of the coherence of the beam, are illustrated by several examples. Emphasis is given to the possibilities associated with modern electronic detectors for this type of imaging. The new techniques implemented at the ESRF that take full advantage of new capabilities, and more particularly that of 'topo-tomography', are presented.

Keywords: imaging; diffraction imaging; X-ray topography.

1. Introduction

X-ray diffraction imaging, historically called X-ray topography, is a 'classical' technique used for the visualization of defects (dislocations, twins, domain walls, inclusions, impurity distribution *etc.*) and macroscopic deformations (curvature, acoustic waves *etc.*) present within the single-crystal sample. The first X-ray topographical experiment dates back to 1931 and was carried out by Berg (1931). The first white-beam topography technique, nowadays the most popular owing to its simplicity, was published by Ramachandran (1944). The first high-resolution diffraction imaging techniques, revealing defects as growth striations or dislocations in crystals, were introduced in the 1950s with double-crystal topography by Bond & Andrews (1952) and the well known 'section' and 'projection' topography by Lang (1958, 1959). It took 15 more years before synchrotron radiation became available for condensed-matter scientists and Tuomi *et al.* (1974) obtained the first white-beam topographs, using synchrotron radiation from HASYLAB at DESY, Hamburg, a second-generation source. Since then, numerous dedicated synchrotron radiation sources have been constructed, providing beams with higher quality and stability.

The modern third-generation synchrotron radiation sources offer enhanced possibilities with respect to previous synchrotron diffraction imaging work. This is true for all the variants of diffraction imaging techniques [white or (quasi)-monochromatic beam topography, using flat or bendable monochromators, peak, flank or 'weak beam' topography]. Some of them are quantitative improvements but others allow detecting qualitatively new effects. These improvements and enhanced possibilities, as well as new techniques taking full advantage of the original features of third-generation sources, are presented and illustrated through examples taken from experiments carried out at the ID19 beamline of the European Synchrotron Radiation Facility (ESRF) in Grenoble, France.

This paper shows how diffraction topography, which is a relatively 'old' technique, has been renewed by the modern sources of synchrotron radiation. The future of this kind of technique will be discussed.

2. Diffraction imaging on modern synchrotron radiation sources: improved or new features

2.1. Improvements with respect to previous synchrotron radiation diffraction imaging work

The quantitative improvements with respect to previous synchrotron radiation imaging work are mainly related to the considerable increase of (*a*) the available photon flux and (*b*) the wavelength spectrum.

The *high intensity* allows one to exploit weak reflections, to use 'weak beam'-type techniques, or to investigate thin layers. Very short exposure times are possible (down to about 0.01 s at ID19, and basically limited by the present fast shutters). This permits one to carry out dynamic experiments, and to look at evolving phenomena (time scale of a few 10^{-2} s). Rapidly changing processes (in the 10^{-8}–10^{-2} s range) may be investigated under the condition that they are periodic. In this case, stroboscopic diffraction imaging may be used, either by exploiting the time structure of the produced synchrotron radiation or by inserting a mechanical chopper into the beam. In addition, the available high intensity allows one to use rather complex sample environment devices (high and low temperatures, electrical and magnetic fields, mechanical traction *etc.*).

The *extended wavelength range* of the radiation produced at large synchrotrons makes high energies accessible. This may be of importance for the above-mentioned sample environment devices, but is essential for the investigation of bulky and strongly absorbing samples.

2.2. New features associated with the modern synchrotron radiation sources

New features with respect to previous synchrotron radiation imaging work are related to the considerable decrease of the angular extent of the source size as seen from a point in the specimen (which is about 0.04″ vertically and 0.2″ horizontally for the ESRF 'long' beamline ID19, devoted to imaging).

This entails qualitatively new effects:

(*a*) Firstly, this small angular source size results in a very high geometrical resolution. This implies that the sample-to-detector distance can be varied at will in the metre range without appreciable blurring of the image, and can therefore be used as an additional experimental parameter. For instance, the discontinuous change in distortion associated with magnetic domains (Medrano *et al.*, 1999), or implanted layers in a piezoelectric crystal (Rejmánková *et al.*, 1996), could be directly measured. It was also possible to observe a focusing effect due to continuous spatial variations of lattice plane orientation. This effect was visualized in the cases of the images of single dislocations (Zontone *et al.*, 1996), elastic resonance patterns (Matsouli *et al.*, 1998, 1999), or wafer bonded samples (Baruchel *et al.*, 1999). The possible large sample-to-detector distances are also of practical importance, *e.g.* for the reduction of background radiation.

(*b*) Secondly, this very small angular source size also results in a considerable lateral coherence length. Propagation of a partially coherent diffracted beam, *i.e.* Fresnel diffraction, can turn variations of the phase of the diffracted beam into changes in intensity, and hence contrast. In the case of a periodic spatial variation of the phase such as produced by inverted ferroelectric domains, this provides the possibility of measuring the difference in phase of the beam diffracted by these domains. This allows the extraction of information about the actual way these domains are matched with respect to the other. In this way, atomic scale structural information may be extracted from macroscopic phase information. The investigation of the combination of Bragg and Fresnel diffraction, *i.e.* the influence of

phase changes (within or outside the crystal) on the amplitudes of the Bragg diffracted waves, appears very promising.

However, the tremendous progress in X-ray diffraction imaging over the last years is not solely due to the improvements of modern synchrotron radiation sources. A considerable contribution should be attributed to the progress in the technology of electronic detectors. Diffraction imaging traditionally uses films and nuclear plates as recording media. They combine high spatial resolution (down to a micrometre) with a large field of view (from centimetres to metres). Nowadays, an increasing number of CCD cameras (two-dimensional detectors) with different dynamic range, sensitivity, noise, effective pixel size and field of view are used. Concerning the important parameters effective pixel size or resolution, they may already surpass that of X-ray films and plates, but at the price of a very limited field of view. However, many applications/measurements are only possible when using these modern electronic two-dimensional detectors. This will become evident in some of the examples presented in the following section.

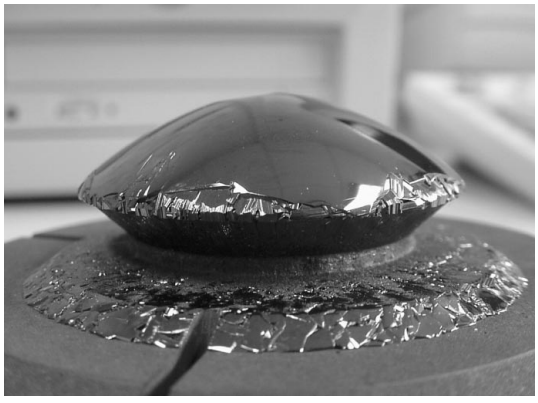

Figure 1
Photograph showing an SiC ingot (LETI, Grenoble). The diameter of the largest part of the ingot is 3.5 cm.

3. Examples of diffraction imaging using modern synchrotron radiation features

3.1. Characterization of as-grown 4H-SiC ingots (Pernot *et al.*, 2001)

A first straightforward example of an X-ray diffraction topographical experiment requiring high energies and high intensity is the study of bulky samples. Taking advantage of the high geometrical resolution, it is possible to investigate (with short exposure times) entire crystal ingots directly after their growth (Fig. 1). This allows the characterization of their structural quality and of the lattice defects they contain, prior to cutting the slices needed for later applications. A general problem in X-ray topography (and other imaging techniques) is that only a two-dimensional projection of the three-dimensional object is produced. One possibility for overcoming this limitation and to obtain information about the spatial distribution of the defects in the investigated crystal ingot is to use a special variant of the technique *i.e.* section topography, where one dimension of the incident beam is restricted by a slit.

Fig. 2(*b*) presents a set of section topographs of the central part of an ingot recorded using four different geometries described in Fig. 2(*a*). The presence of the polycrystal surrounding the main crystal produces additional contrast at the periphery of the ingot. Micropipes images can be observed mainly in the lower-left part of the first image of Fig. 2(*b*); however, the central part of the ingot

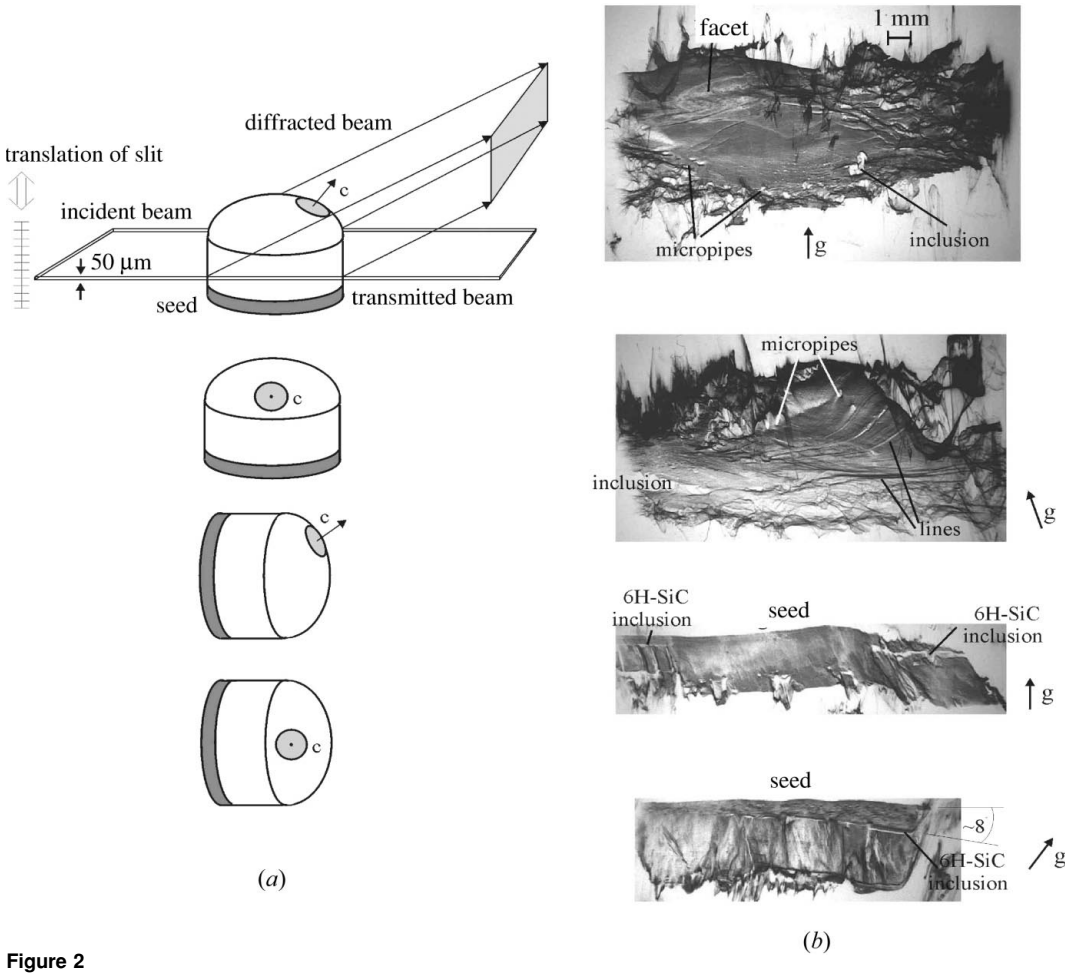

Figure 2
(*a*) Experimental arrangement for section topography with the possibility of modifying the incident beam position on the sample by the displacement of the slit. Four geometries of an ingot with respect to the facet perpendicular to the *c*-axis (marked by the grey circle/ellipse on the top of the ingot) are presented. (*b*) Typical section topographs of an ingot recorded for the four different experimental geometries described in (*a*). The vector **g** is the projection of the diffraction vector onto the film.

remains almost defect-free. The facet, *i.e.* the natural surface perpendicular to the *c*-axis, observed as a light elliptical feature in the upper-left region of the section, constitutes a high-crystalline-quality region. The seed–crystal interface is hardly visible both in the third and fourth sections indicating a smooth start of the crystal growth. However, inclusions of other polytypes, 6H-SiC or 15R-SiC, can be observed close to the seed. The inclusions start to grow from one side of the ingot and propagate with an angle of 8° with respect to the horizontal ingot axis until they reach the opposite side. The inclusions originate a number of planar defects that propagate along the vertical ingot axis, up to the natural crystal surface. Consequently, these inclusions deteriorate considerably the crystalline quality. This polytype switching is related to the 8° off-axis orientation of the seed. By avoiding the instabilities occurring at the beginning of the crystal growth it is possible to dramatically increase the useful volume of the grown crystals. Fig. 3 shows detailed views, corresponding to two different moments during the crystal growth. In Fig. 3(*a*) the slit position was set at the level of the ingot dome (this corresponds to almost the end of the crystal growth) and in Fig. 3(*b*) the section topograph was recorded at the level of the crystal seed (the beginning of the crystal growth). The distance between these two positions of the slit was about 1 cm.

This example shows that the investigation of defects inside bulky ingots of 4H-SiC, without slicing it, can be performed using a very simple set-up: white-beam section topography in transmission. This study allows a correlation between growth conditions (seed orientation, temperature gradient, gas pressure *etc.*) and defects to be established.

3.2. Defects in quasicrystals

Quasicrystals are non-crystalline materials with long-range translational and rotational order, but no three-dimensional periodicity. These materials exhibit five-, eight- or ten-fold symmetry axes not existing in periodic structures, show sharp diffraction peaks and display unusual physical properties. An important question which was considered from the very beginning of 'quasicrystallography' is how perfect quasicrystals are (and can be) and which kind of defects do they contain? X-ray topography under weak beam conditions ('weak beam topography'), in combination with phase-sensitive radiography (Cloetens *et al.*, 1996), considerably contributed to providing an answer through the visualization of defects (on the micrometric scale) in quasicrystals and the analysis of their contrast behaviour (Mancini *et al.*, 1998; Gastaldi *et al.*, 1999; Klein *et al.*, 2001).

Figs. 4(*a*)–4(*c*) show topographs recorded on the peak of the rocking curve for different sample-to-film distances: no substantial changes of the mostly loop-shaped contrasts are visible. It is important to remember that the relation between the defect and its diffraction image on the topograph is a complicated one. Consequently, a loop-shaped defect image does not necessarily indicate that the defects are loop-shaped. This becomes evident in Figs. 5(*a*)–5(*c*). They show 'weak-beam' topographs taken on a wing of the rocking curve (angular distance from peak = 2.4 arcmin) for various sample-to-detector distances. On these images important changes of the defect contrasts occur, and many loops gradually transform into a double line contrast. Keeping in mind that under weak-beam conditions the strongly deformed zones close to the defect centres or defect boundary are those which contribute to the image, the images in Fig. 5(*c*) should be closer to the actual shape of the defect. This is confirmed in Fig. 6, where a topograph of a small sample region is compared with a phase contrast radiograph showing pores and precipitates (platelet-like shaped or almost spherical). The contrast associated with pores is clearer in quasicrystals with no precipitates (Fig. 7). In this case the topographical image (Fig. 7*a*) exhibits a two-lobe contrast similar to that known from spherical precipitates in crystals.

The above example demonstrates that by using 'weak-beam topography' it is possible to image strongly deformed zones close to

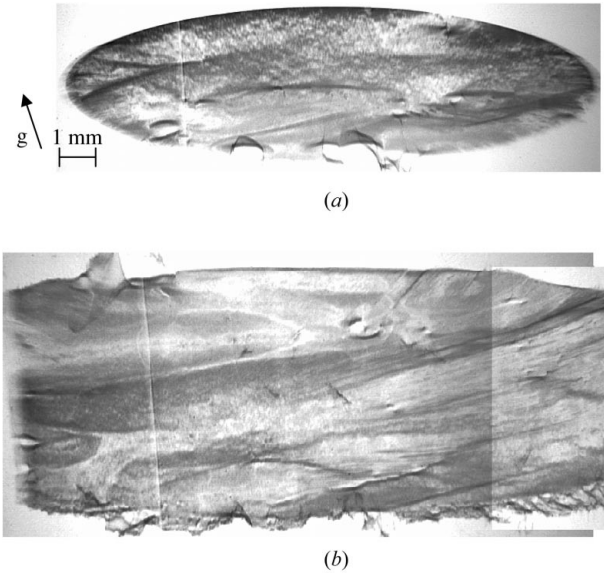

Figure 3
Section topographs recorded with different positions of the slit, corresponding to different moments during the crystal growth. (*a*) Slit set at the level of the ingot dome (near to the end of the crystal growth). (*b*) Section recorded at the level of the crystal seed (the beginning of the crystal growth). The distance between these two positions of the slit was about 1 cm.

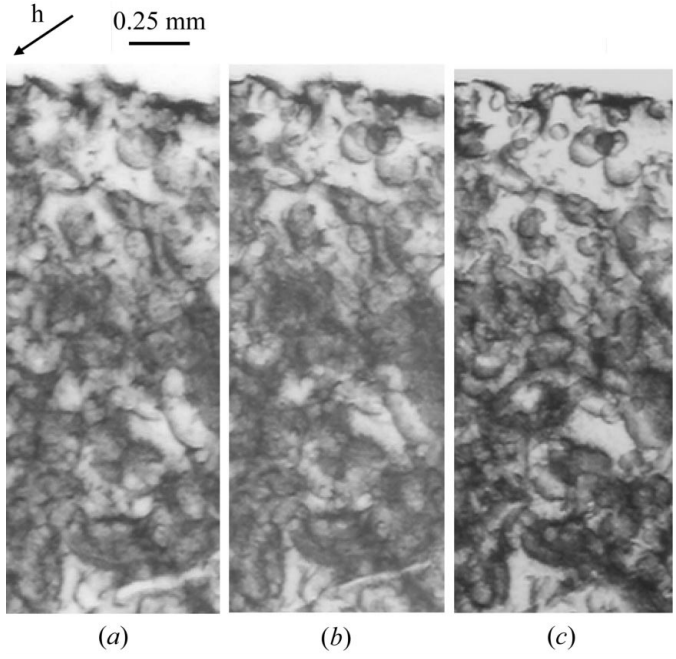

Figure 4
Monochromatic beam (Si 111 double-monochromator) topographs taken on the peak of the rocking curve at different sample-to-detector distances, $\lambda = 0.559$ Å, $\tau^2(0\,0\,0\,20\,0)$ reflection, Czochralski-grown quasicrystal $Al_{69.7}Mn_{22.7}Pd_{7.6}$, annealed for 96 h at 1023 K, sample-to-detector distance 35 cm (*a*), 15 cm (*b*), 1.7 cm (*c*). **h** indicates the direction of the diffraction vector.

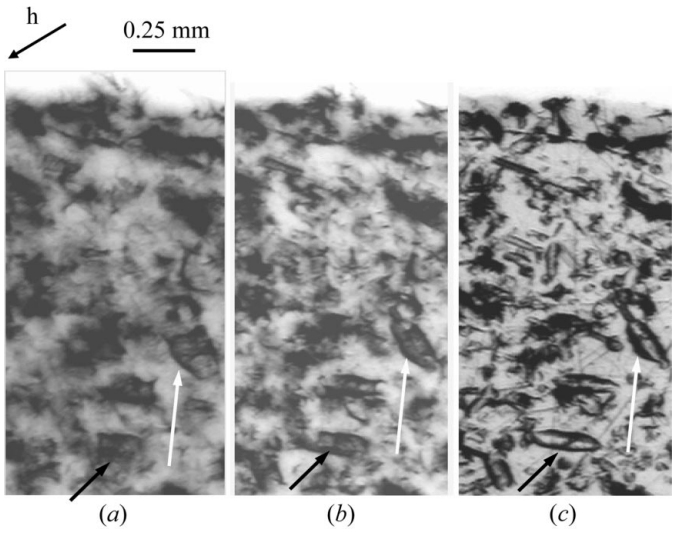

Figure 5
As Fig. 4, but 'weak beam' topographs, taken on a wing of the rocking curve with an angular distance from the peak of 2.4 arcmin, $\lambda = 0.559$ Å, τ^2 (0 0 0 $\bar{2}$ 0 0), sample-to-detector distances 35 cm (*a*), 15 cm (*b*), 2.8 cm (*c*).

the defect cores or defect boundary. A deeper understanding of the nature of the defects and their associated deformation (on the micrometric scale) in quasicrystals resulted from the combination with phase-sensitive radiography, and the use of the sample-to-detector distance as a parameter.

3.3. 180° Antiferromagnetic domains in CoF_2 (Baruchel *et al.*, 2001)

CoF_2 is antiferromagnetic below $T_N \simeq 37$ K. Magnetic moments of opposite sign, directed along the *c*-axis, are located at the corners and the centre of the tetragonal unit cell, respectively. These two sites, although equivalent, are not related by a lattice translation (the fluorine environment being rotated by 90° around the *c*-axis), which leads to two possible 180° antiferromagnetic domains, and to the existence of piezomagnetism.

The piezomagnetic strain induced by an applied magnetic field is of opposite sign in the two kinds of antiferromagnetic domains. This effect is used to visualize, by X-ray diffraction imaging, these domains in a CoF_2 crystal at temperatures between 10 K and 40 K, by applying external magnetic fields up to 0.4 T. Moderate magnetic fields are chosen to ensure that the domain structure is not modified. However, this implies that the distortion remains weak

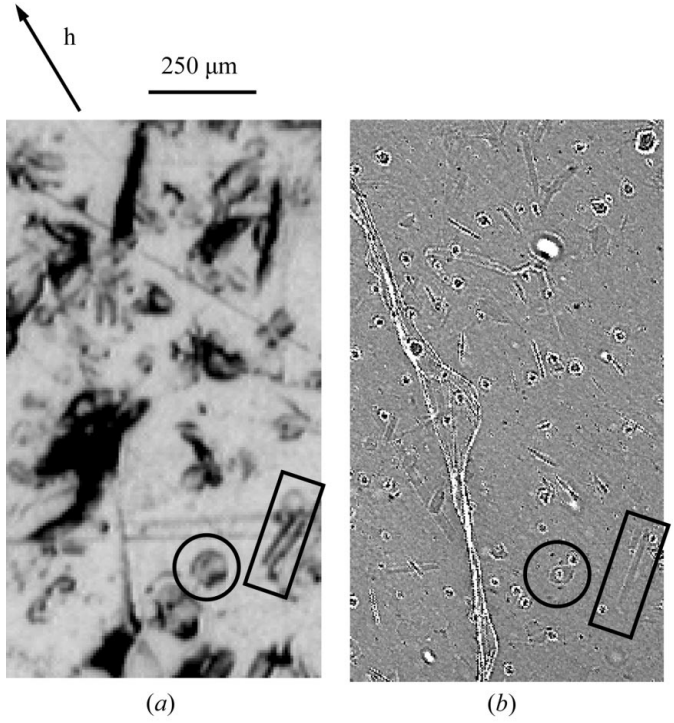

Figure 6
Comparison of a weak-beam topograph (*a*) and a phase-contrast image (*b*). A platelet-like shaped and (almost) spherical precipitate are indicated.

($<10^{-6}$). The experiment is therefore performed by first recording images with and without an applied field on a CCD camera equipped with an X-ray scintillator. These images are shown in Fig. 8, and display no big difference. However, when subtracting the two images

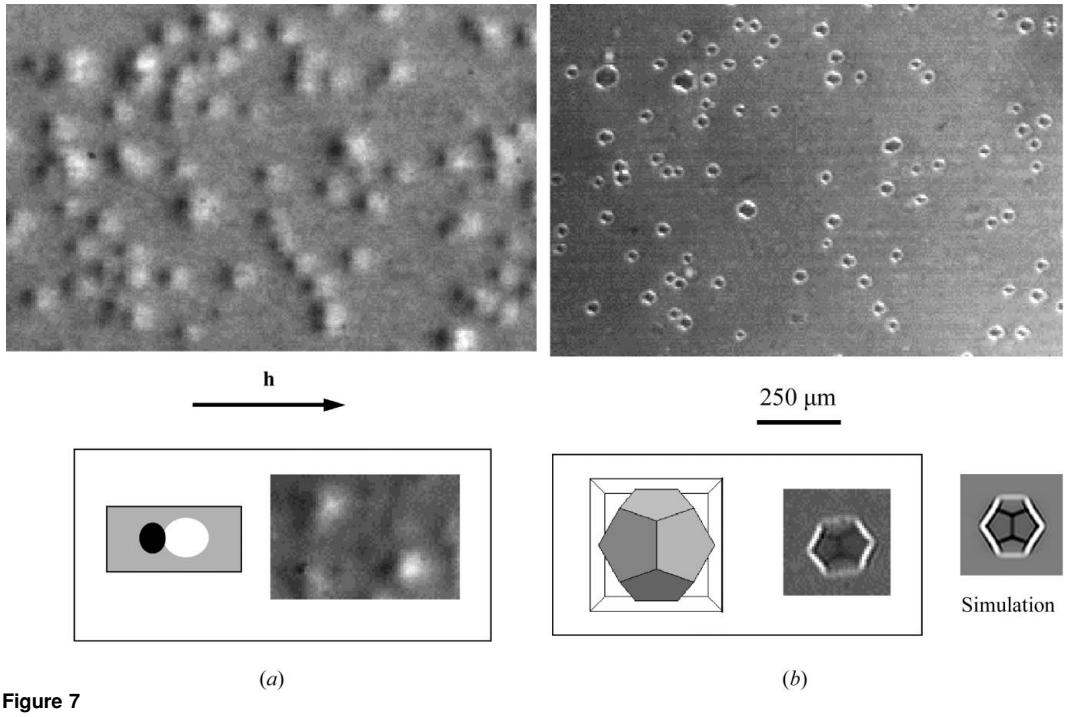

Figure 7
Comparison of an X-ray topograph (*a*) and a phase-contrast image (*b*) of a non-annealed sample ($Al_{68.6}Pd_{24.7}Mn_{6.7}$) of rather good quality containing pores. A one-to-one correspondence of double-lobe contrasts and pores is visible. Sample-to-detector distance = 20 cm.

a domain-related contrast is then observed (Fig. 9), which only amounts to less than 10% of the matrix intensity, and is hardly visible without the subtraction operation. The induced strain (*a*) increases with increasing magnetic field, (*b*) reverses when the direction of the magnetic field is reversed and (*c*) decreases with increasing temperature, vanishing at T_N.

The use of the subtraction of images affords the possibility of investigating weak phenomena, which provide only very weak contrast changes in X-ray topographical images. This subtraction practically necessitates the electronic recording of the images. This corresponds to the present evolution where films and nuclear plates are being replaced, in many cases (but not all of them!) by CCD cameras.

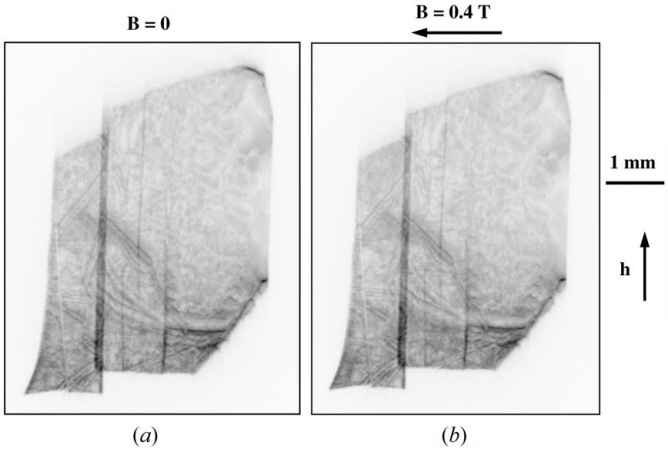

Figure 8
White-beam topograph of a CoF_2 crystal at $T = 10$ K without (*a*) and with (*b*) magnetic field. 020 reflection, $\lambda = 0.22$ Å.

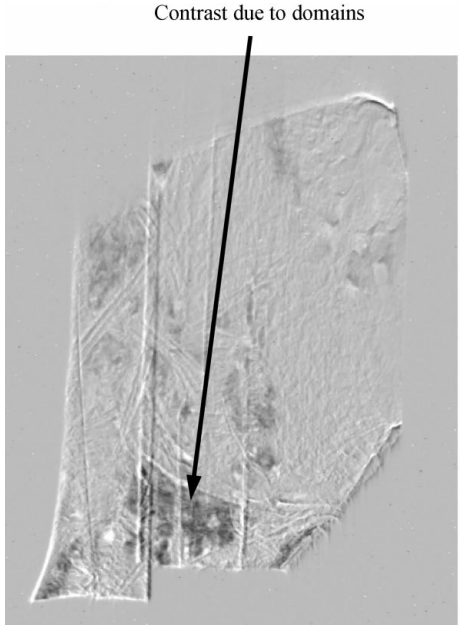

Figure 9
Difference image resulting from the subtraction of Figs. 8(*a*) and 8(*b*), which reveals the contrast associated with the 180° antiferromagnetic domains.

3.4. Direct mapping of the vibration modes of piezoelectric devices (Capelle *et al.*, 2001)

Observations of another type of phenomenon, piezoelectric vibrations, greatly benefit from the variation of the sample-to-detector distance, coupled with X-ray stroboscopic diffraction topography. Further examples for the utilization of this new 'distance' parameter may be found by Baruchel *et al.* (1999).

Piezoelectric devices are widely used in electronics, among others in computers or in mobile telephones. The understanding of the vibration modes in quartz resonators is important for a correct

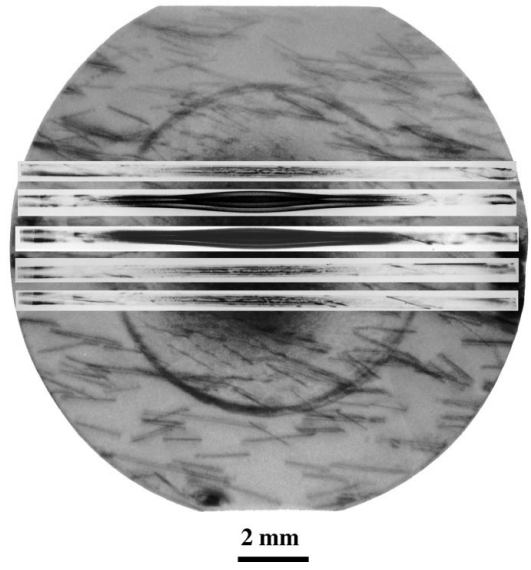

Figure 10
White-beam topograph of a plano-convex quartz resonator with superposed section topographs. The sample-to-detector distance is about 5 cm, $(1\bar{2}10)$ reflection, $\lambda \simeq 0.07$ nm, image width = 15 mm.

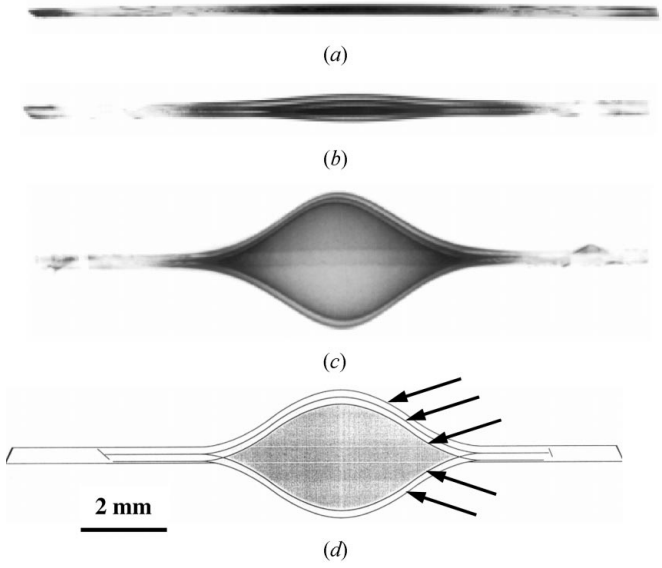

Figure 11
Series of stroboscopic section topographs in the case of the fifth overtone, taken at different sample-to-detector distances of (*a*) about 5 cm, (*b*) 70 cm, (*c*) 180 cm (but in addition taken with a higher excitation level). In (*d*) the five contrast lines are marked: three on one side, two on the other.

adjustment of their ultra-acoustic properties. Stroboscopic topography allows to 'freeze' the vibration at a given moment of the period. X-ray topography is a unique method to directly visualize the vibration modes, to draw a map of the deformation, and to measure the physical characteristics of the ultra-acoustic wave. An image of the whole device can be recorded by using white-beam projection topography; the complementary, and important, depth information is obtained by applying section topography. The use of large sample-to-detector distances allows, in this last case, a considerable 'magnification' to be reached, leading to an increased sensitivity. In this way a comparison between the experimental quantitative measurements and theoretical values of the amplitude of the vibration is possible.

Fig. 10 shows a white-beam topograph of a plano-convex quartz resonator with superposed section topographs taken at a rather short sample-to-detector distance. It is difficult to resolve the detail in the section topographs. By increasing the sample-to-detector distance the images widen and the detail, in the form of fringes, becomes visible (Fig. 11). If a fifth overtone of a shear mode with vibrations in planes parallel to the (plane) oscillator surface is excited, the number of half acoustic wavelengths occurring in the thickness of the resonator is five. This results in five fringes in the topograph, which are visible in Figs. 11(*c*) and 11(*d*). The origin of these fringes is a deviation of the radiation reflected in regions with maximum lattice planes rotations and its focalization after the propagation from the sample to the detector (Matsouli *et al.*, 1998, 1999; Baruchel *et al.*, 1999).

The combination of stroboscopy, section topography and large sample-to-detector distances is therefore shown to allow quantitative measurements of the amplitudes or attenuation coefficients of the acoustic vibrations modes, and consequently their comparison with theoretical model predictions.

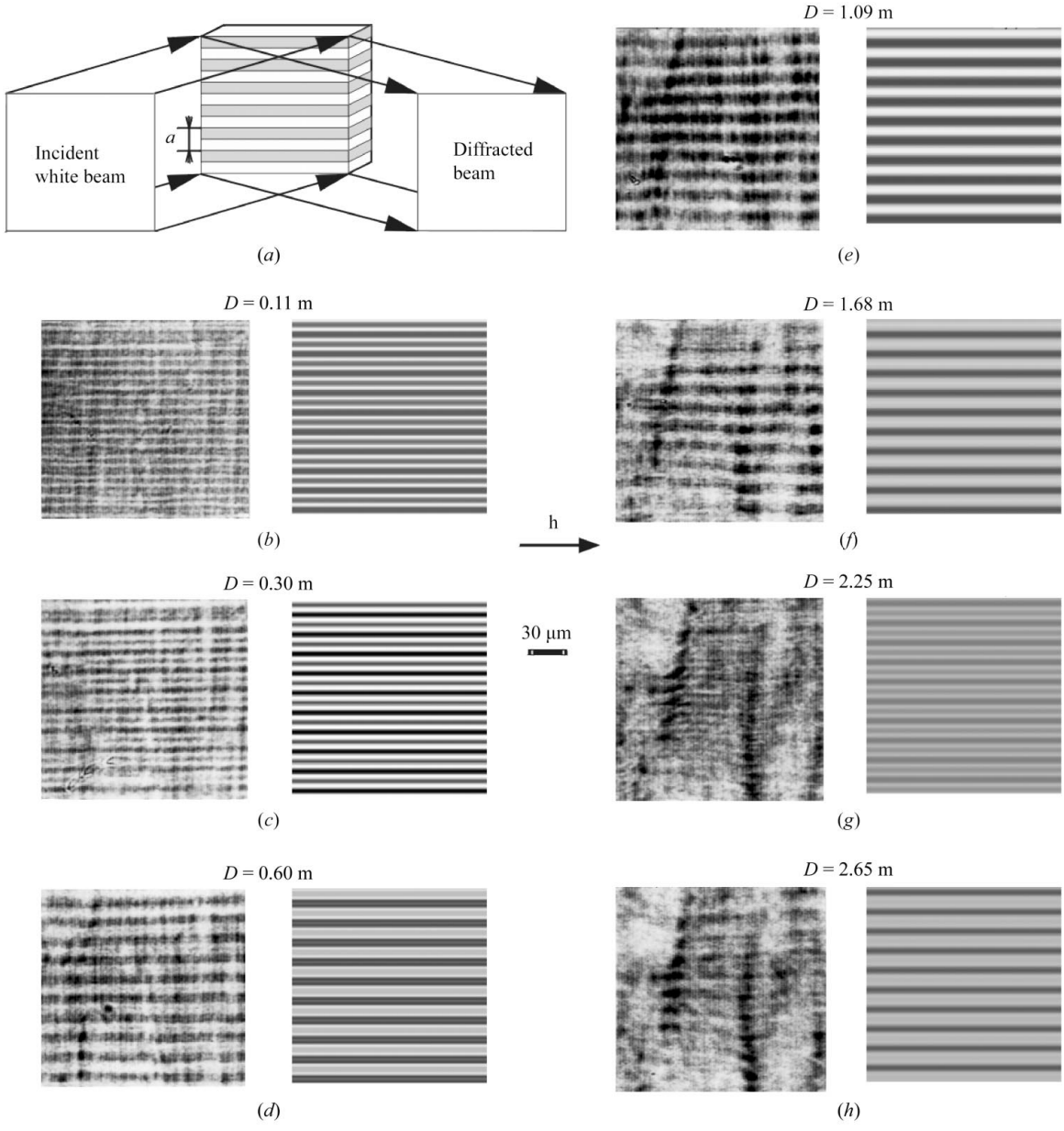

Figure 12
(*a*) Experimental set-up: white-beam topography in reflection. (*b*)–(*h*) Experimental and simulated images of 006 reflection of a periodically poled lithium niobate (period 14.8 μm) for different sample-to-detector distances *D*.

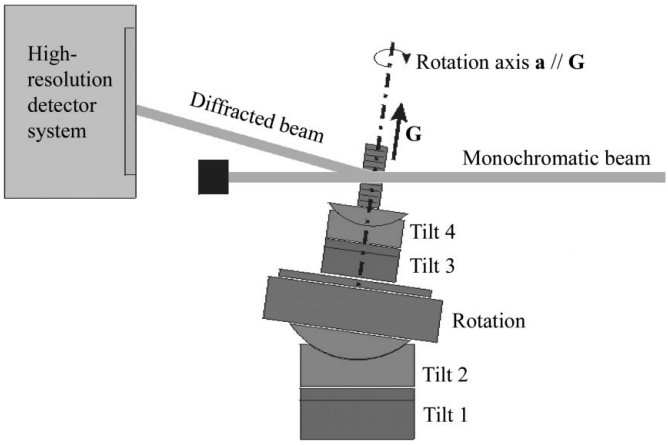

Figure 13
Experimental set-up used for topo-tomographic data acquisition. During the tomographic scan, the crystal is turned around the rotation axis **a** (angle ω). The crystal has to be aligned such that the diffraction vector **G** is parallel to **a**.

3.5. Visualization and matching determination of 180° ferroelectric domains

The ferroelectric domains investigation presented in this paragraph is an example of the use, in diffraction topography, of the considerable lateral coherence length of the beam. It uses a combination of Bragg and Fresnel diffraction.

Lithium niobate, KTP and KTA crystals can achieve optical second-harmonic generation with enhanced efficiency when a periodic reversal of the sign of the non-linear optical coefficient d_{33} occurs in the phase-matching period. This periodically inverted domain structure can be produced by applying an external electric field using patterned electrodes. Fresnel and Bragg diffraction were used simultaneously to visualize these ferroelectric domains. In this case no usual topographic contrast is expected. Spectacular effects result from the phase contribution to Bragg-diffraction imaging in periodically poled lithium niobate (Rejmánková-Pernot *et al.*, 1998) and KTA crystals (Pernot-Rejmánková *et al.*, 2000). Bragg diffraction introduces a phase shift between the waves diffracted by adjacent domains. It mainly originates from the phase shift between the structure factors of oppositely poled regions. Fresnel diffraction determines the resulting intensity distribution after free space propagation. This phase difference is thus extracted from images recorded at different distances from the sample. Fig. 12 shows a scheme of the white-beam experimental set-up and the images of a periodically poled lithium niobate crystal (period = 14.8 μm, 006 reflection, E = 12.4 keV). The comparison of experiment and simulation (shown on the right-hand side of the corresponding experimental image) allows the magnitude of the phase shift involved to be quantitatively determined. The phase modulation used for the simulation is a periodic rectangular profile. The calculated and measured phase shifts are in very good agreement, being both equal to 140°. This approach, made possible by the large spatial coherence of the X-ray beam, provides, in addition, important quantitative information about atom displacements at the ferroelectric wall.

4. New techniques: topo-tomography

New techniques are emerging which take full advantage of the described new capabilities. Among them, the monochromator bending allows to compensate for sample curvature and/or for the limitations of dispersive set-ups (Altin *et al.*, 2002), and the sample rocking combined with a high-resolution camera leads to rock-scan mappings with micrometric resolution (Lübbert *et al.*, 2000). Topo-tomography, which combines synchrotron-based diffraction topography with microtomography, allows a three-dimensional imaging of the strain-field related to defects to be achieved (Ludwig *et al.*, 2001). In this way an additional method became available for overcoming the above-mentioned limitation of X-ray topography, which produces two-dimensional projection of a three-dimensional object. Topo-tomography was used to produce a three-dimensional visualization of the three-dimensional dislocation structure in a synthetic diamond.

The distortions of the crystal lattice associated with the individual dislocations give rise, in the low-absorption case, to locally enhanced X-ray reflectivity and can be observed as line-shaped dark contrasts [so-called 'direct image' contrast (Bowen & Tanner, 1998)]. Provided that the direct image is the dominant contrast mechanism, the intensity distribution in the diffraction image is a good approximation

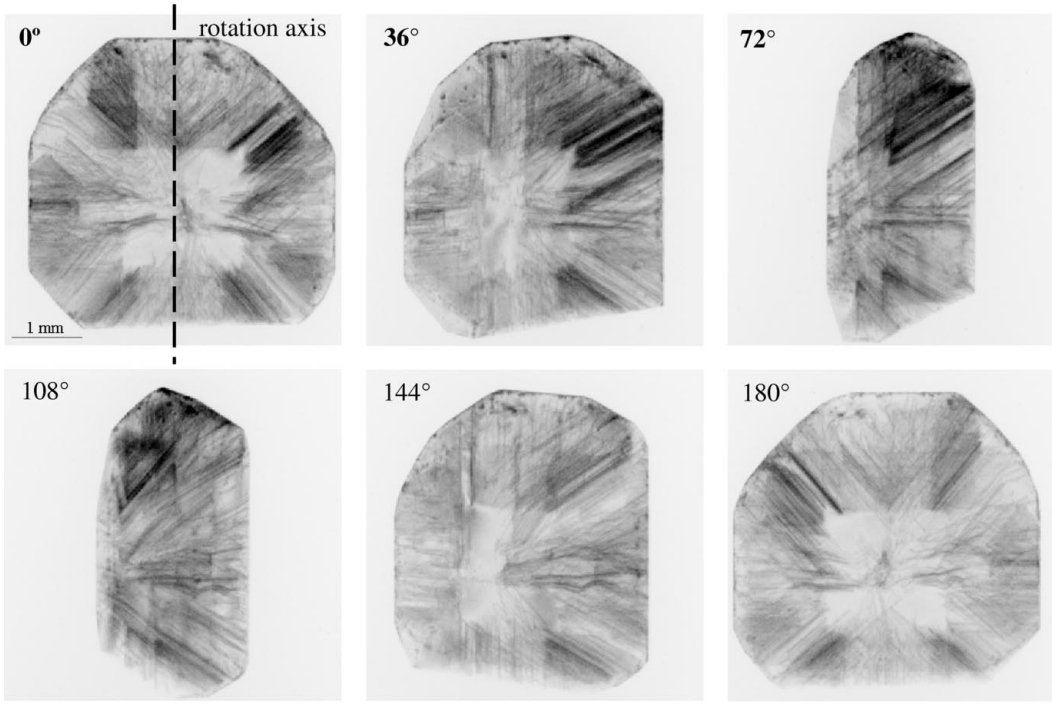

Figure 14
Series of six out of the 500 diffraction topographs recorded from a 7 mm × 7 mm × 2 mm synthetic diamond sample.

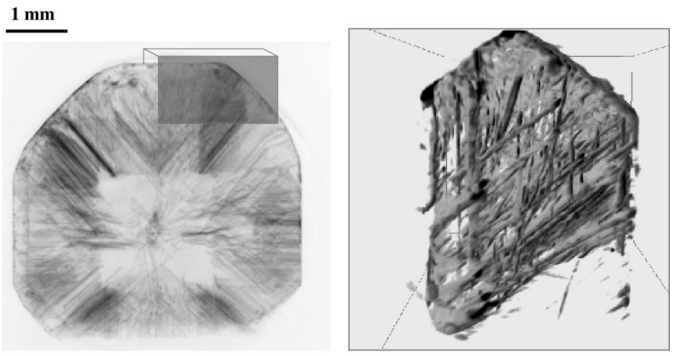

(*a*) (*b*)

Figure 15
(*a*) Conventional X-ray diffraction topograph (two-dimensional) of diamond sample (dark lines mean more intensity). (*b*) Three-dimensional rendition of the small part of the crystal indicated in (*a*).

to a two-dimensional projection of the local reflectivity along the direction of the diffracted beam. Consequently, if one succeeds in measuring a large number of such projections while turning the sample around a fixed rotation axis, the principles of computed tomography can be applied in order to reconstruct the unknown three-dimensional distribution of the local reflectivity. However, compared with conventional absorption tomography, there is the additional constraint that the crystal, during its turn around the rotation axis, has to stay in diffraction for a given reflection. This can be achieved by an experimental set-up as depicted in Fig. 13, which allows for precise alignment of the rotation axis **a** and the reciprocal lattice vector **G**, associated with the chosen sample reflection. Fig. 14 shows six out of the 500 diffraction topographs recorded from a 7 mm $\times$ 7 mm $\times$ 2 mm synthetic diamond sample. As can be seen from these diffraction images, the crystal contains a large number of individual dislocations, which superimpose in this single projection. Applying a simple intensity threshold to the three-dimensional dataset, one can easily visualize the three-dimensional arrangement of the dislocation lines with standard volume-rendering software. Such a three-dimensional rendition of a small part of the crystal (indicated by the box in Fig. 15*a*) is finally shown in Fig. 15(*b*). One can observe different families of line-shaped contrasts, which correspond to dislocations with preferential orientations in the crystal lattice.

5. Conclusions

X-ray diffraction imaging is today a 'classical' technique. It is, of course, still very useful in its original form for characterizing single crystals of good crystalline quality. However, in addition, the association with modern synchrotron radiation sources has renewed it. It is presently partly used to follow *in situ* and/or real-time phenomena, *i.e.* the evolution of a process as a function of an external parameter (time, temperature, electric or magnetic field, stress *etc.*). Further examples may be found by Medrano *et al.* (2001), Zolotoyabko *et al.* (1998), Sauer *et al.* (1999) and Polcarová *et al.* (1999*a*,*b*).

Most of the examples presented in the present paper were impossible to perform before the advent of third-generation synchrotron radiation sources. They show that there are new applications of diffraction imaging techniques. The developments in the future will surely take advantage of (*a*) the coherence properties of the beams (combination of Bragg and Fresnel diffraction), (*b*) the *in situ* observations under complex sample environment, and (*c*) the increased use of electronic two-dimensional detectors.

References

Altin, D., Härtwig, J., Köhler, R., Ludwig, W., Ohler, M. & Klein, H. (2002). *J. Appl. Cryst.* Submitted.
Baruchel, J., Cloetens, P., Härtwig, J. & Schlenker, M. (1999). *Philos. Trans. R. Soc. London Ser. A*, **357**, 2741.
Baruchel, J., de Camargo, P. C., Mazzaro, I., Nogues, J. & de Oliveira, A. (2001). *J. Phys. D*, **34**, A114–A116.
Berg, W. F. (1931). *Naturwissenschaften*, **19**, 391–396.
Bond, W. L. & Andrews, J. (1952). *Am. Miner.* **37**, 622–632.
Bowen, D. K. & Tanner, B. K. (1998). *High-Resolution X-ray Diffractometry and Topography.* London: Taylor and Francis.
Capelle, B., Détaint, J. & Epelboin, Y. (2001). *J. Appl. Cryst.* **34**, 625–629.
Cloetens, P., Barrett, R., Baruchel, J., Guigay, J.-P. & Schlenker, M. (1996). *J. Phys. D*, **29**, 133–146.
Gastaldi, J., Mancini, L., Reinier, E., Ludwig, W., Janot, C., Baruchel, J., Härtwig, J. & Schlenker, M. (1999). *J. Phys. D*, **32**, A152–A159.
Klein, H., Agliozzo, S., Gastaldi, J., Härtwig, J. & Baruchel, J. (2001). *J. Phys. D*, **34**, A98–A102.
Lang, A. R. (1958). *J. Appl. Phys.* **29**, 597–598.
Lang, A. R. (1959). *Acta Cryst.* **12**, 249–250.
Lübbert, D., Baumbach, G. T., Härtwig, J., Boller, E. & Pernot, E. (2000). *Nucl. Instrum. Methods B*, **160**, 521–527.
Ludwig, W., Cloetens, P., Härtwig, J., Baruchel, J., Hamelin, B. & Bastie, P. (2001). *J. Appl. Cryst.* **34**, 602–207.
Mancini, L., Reinier, E., Cloetens, P., Gastaldi, J., Härtwig, J., Schlenker, M. & Baruchel, J. (1998). *Philos. Mag. A*, **78**, 1175.
Matsouli, I., Kvardakov, V., Espeso, J., Chabert, L. & Baruchel, J. (1998). *J. Phys. D*, **31**, 1478–1486.
Matsouli, I., Pernot, E., Baruchel, J., Kvardakov, V., Chabert, L. & Palmer, S. B. (1999). *J. Phys. D*, **32**, A104–A1108.
Medrano, C., Pernot, E., Espeso, J. I., Boller, E., Lorut, F. & Baruchel, J. (2001). *J. Magn. Magn. Mater.* **226**/**230**, 623–625.
Medrano, C., Schlenker, M., Baruchel, J., Espeso, J. I. & Miyamoto, Y. (1999). *Phys. Rev. B*, **59**, 1185–1195.
Pernot, E., Pernot-Rejmánková, P., Anikin, M., Pelissier, B., Moulin, C. & Madar, R. (2001). *J. Phys. D*, **34**, A136–A139.
Pernot-Rejmánková, P., Thomas, P. A., Cloetens, P., Lorut, F., Baruchel, J., Hu, Z. W. & Rosenman, G. (2000). *J. Appl. Cryst.* **33**, 1149–1153.
Polcarová, M., Brádler, J., Gemplerová, J., Jacques, A. & George, A. (1999*a*). *Appl. Phys.* **32**, A109–A113.
Polcarová, M., Brádler, J., Gemplerová, J., Jacques, A. & George, A. (1999*b*). *Philos. Trans. R. Soc. London Ser. A*, **357**, 2701–2705.
Ramachandran, G. N. (1944). *Proc. Ind. Acad. Sci.* A**19**, 280–292.
Rejmánková, P., Baruchel, J. & Moretti, P. (1996). *Physica B*, **226**, 293–303.
Rejmánková-Pernot, P., Cloetens, P., Baruchel, J., Guigay, J.-P. & Moretti, P. (1998). *Phys. Rev. Lett.* **81**, 3435–3438.
Sauer, W., Streibl, M., Metzger, T. H., Haubrich, A. G. C., Manus, S., Wixforth, A., Peisl, J., Mazuelas, A., Härtwig, J. & Baruchel, J. (1999). *Appl. Phys. Lett.* **75**, 1709–1711.
Tuomi, T., Naukkarinen, K. & Rabe, P. (1974). *Phys. Status Solidi A*, **25**, 93–106.
Zolotoyabko, E., Shilo, D., Sauer, W., Pernot, E. & Baruchel, J. (1998). *Appl. Phys. Lett.* **73**, 2278–2280.
Zontone, F., Mancini, L., Barrett, R., Baruchel, J., Härtwig, J. & Epelboin, Y. (1996). *J. Synchrotron Rad.* **3**, 173–184.